Characterization of the Stability of Indium Tin Oxide and Functional Layers for Semitransparent Back-Contact Applications on Cu(in,Ga)Se₂ Solar Cells

Robert Fonoll-Rubio,* Marcel Placidi,* Torsten Hoelscher, Angelica Thomere, Zacharie Jehl Li-Kao, Maxim Guc, Victor Izquierdo-Roca, Roland Scheer, and Alejandro Pérez-Rodríguez

Herein, a detailed study of the stability of different ITO-based back-contact configurations (including bare ITO contacts and contacts functionalized with nanometric Mo, MoSe₂, and MoS₂ layers) under the coevaporation processes developed for the synthesis of high-efficiency Cu(In,Ga)Se₂ (CIGSe) solar cells is reported. The results show that bare ITO layers can be used as efficient back contacts for coevaporation process temperatures of 480 °C. However, higher temperatures produce an amorphous In–Se phase at the ITO surface that reduces the contacts transparency in the visible region. This is accompanied by degradation of the solar cells' efficiency. Inclusion of a Mo functional layer leads to the formation of a MoSe₂ interfacial phase during the coevaporation process, which improves the cells' efficiency, achieving device efficiencies similar to those obtained with reference solar cells fabricated with standard Mo back contacts. Optimization of the initial Mo layer thickness improves the contact transparency, achieving contacts with an optical transparency of 50% in the visible region. This is accompanied by a relevant decrease in back reflectivity in the CIGSe devices, confirming the potential of these contact configurations for the development of semitransparent CIGSe devices with improved optical aesthetic quality without compromising the device performance.

1. Introduction

Thin-film photovoltaics (PV) presents numerous advantages such as low material usage, fabrication versatility, and easy integration (e.g., building-integrated PV [BIPV], wearables, internet of things, etc.). Among the nontoxic thin-film absorbers, Cu(In,Ga)Se₂ (CIGSe) has achieved the highest energy conversion efficiency (23.35%) at the laboratory scale[1] and it has been proven viable for large-scale industrial development.[2] Thus, technologies based on CIGSe play an important role in the democratization and integration of PV through mass production of cheap and efficient solar cell devices.

There exists a growing interest in CIGSe solar cells grown on transparent and semitransparent back contacts as this configuration offers different applications such as bifacial devices,[3–7] semitransparent BIPV,[8] and tandem solar cells.[9–12] Focusing on BIPV, it is predicted to achieve a relevant share of the total PV production of electricity in the next years, leading to strong interest in the recent years in the development of semitransparent PV solutions that will allow to achieve a relevant increase in the surface available in the buildings for the generation of BIPV electricity.[8,13] PV can be an integral part of windows,[14] skylights,[15] agrovoltaics,[16] glass-based facades,[17] and other related structures. Currently, semitransparent BIPV products based on amorphous silicon (a-Si) are being commercialized.[8,14,18,19] However, the energy conversion efficiency of a-Si solar cells was stuck around 10%.[18,20,21] Crystalline Si may

R. Fonoll-Rubio, M. Placidi, A. Thomere, M. Guc, V. Izquierdo-Roca, A. Pérez-Rodríguez
Catalonia Institute for Energy Research (IREC)
Jardins de les Dones de Negre 1
08930 Sant Adrià de Besòs-Barcelona, Spain
E-mail: rfonoll@irec.cat; marcel.placidi@upc.edu

The ORCID identification number(s) for the author(s) of this article can be found under https://doi.org/10.1002/solr.202101071.

M. Placidi, Z. J. Li-Kao
Electronic Engineering Department
Polytechnic University of Catalonia (UPC)
Campus Besòs, Av. d'Eduard Maristany, 16, 08930 Barcelona, Spain

T. Hoelscher, R. Scheer
Institute of Physics
Martin-Luther-University (MLU)
von-Danckelmann-Platz, 3, 06120 Halle, Germany

A. Pérez-Rodríguez
IN2UB
Departament d'Enginyeria Electrònica i Biomèdica
Universitat de Barcelona
Carrer de Martí i Franquès 1, 08028 Barcelona, Spain

also be a candidate for BIPV applications due to its high energy conversion efficiency and high level of technological maturity,[18] even if it lacks the potential advantages of thin-film PV technologies for the design of customized modules adapted to the characteristics of the BIPV element. So, CIGSe absorbers offer an alternative for the BIPV market that promises higher efficiencies than a-Si, while keeping the advantages of thin-film PV.

When the solar cell absorber is of opaque thickness, which is the case of high-efficiency CIGSe, the semitransparency of the device is achieved by means of spatial segmentation,[13,22,23] consisting of removing parts of the absorber layer from selected areas. Thus, solar light is absorbed in the regions with the remaining absorber and it is transmitted in the regions where the absorber has been removed. Increasing the space between the absorption regions increases the transparency of the device, but this strategy is limited by the loss of short-circuit current density (J_{SC}) due to reduced photoactive material[13,22] and thus a trade-off efficiency/transparency has to be chosen depending on the final application.

The typical architecture of CIGSe devices consists of a soda-lime glass (SLG) substrate (3 mm), molybdenum back contact (800 nm), CIGSe absorber layer (2 μm), CdS buffer layer (10–60 nm), zinc oxide (i:ZnO), and a transparent conductive oxide (TCO) such as indium tin oxide (ITO) or aluminum-doped zinc oxide (AZO) window layers.[24–27] However, the replacement of the Mo back contact by semitransparent contact configurations based on the use of TCOs, such as ITO, offers different advantages. First, a metallic back contact, such as Mo, reflects the light at the back surface and, in combination with the glass substrate, generates a "mirror effect" when looking at the module from the substrate side, that is, people see their own reflection in the module back side, which compromises the aesthetic quality of the devices for semitransparent BIPV applications. Taking this into account, TCOs provide a drastic reduction of the back-contact reflectance, which improves the aesthetical quality of BIPV products viewed from the interior of the building by avoiding the mirror effect, a relevant point to ensure a higher level of acceptance of these solutions in the BIPV market. In addition, using a transparent back contact allows also to simplify the segmentation process, as in this case only the CIGSe and upper layers have to be removed in the light-transmitting regions. Finally, the use of semitransparent back contacts allows also the development of nonsegmented semitransparent devices that are based on the use of semitransparent absorbers (including wide-bandgap and/or ultrathin absorbers). This is strongly relevant for the development of devices with higher transparency levels and very high optical quality. Availability of optimal semitransparent back contacts is also required for the development of bifacial devices with improved efficiency, as well as for the development of higher-efficiency tandem device configurations using a wide-bandgap chalcogenide top cell.

Replacement of Mo by a semitransparent back contact in chalcopyrite devices has already been demonstrated using ITO,[9,28–31] fluorine-doped SnO₂ (FTO),[9,28,32] AZO,[28,33] and hydrogen-doped In₂O₃ (IOH).[34,35] In some of these cases, high-efficiency devices were obtained by applying bare ITO with a CIGSe coevaporation deposition temperature of 520 °C (efficiency of 15.2%)[28] or bare IOH with a coevaporation deposition temperature of 550 °C (up to 16.1% efficiency in (Ag,Cu)(In,Ga)Se₂ devices and 11% in Cu(In,Ga)Se₂

devices).[34,35] Nevertheless, in the case of CIGSe absorbers on ITO back contacts, the formation of a Ga₂O₃ layer at the TCO/CIGSe interface has been reported by Nakada et al. for deposition temperatures higher than 520 °C,[9,28] and such a layer has been associated with the deterioration of the device performance due to increased resistivity. To solve this problem, implementation of an intermediate functional layer (FL), such as Mo, between the TCO back contact and the CIGSe absorber has been proposed to avoid the formation of the Ga₂O₃ layer.[9] While the implementation of an FL on TCO back contacts is no novelty, the impact of the absorber fabrication process on the back contact and on the optical properties of the FL/TCO back-contact structure has not been deeply studied. Only a deterioration of the transparency of the ITO back contact is reported after deposition of a CuGaSe₂ absorber film,[31] but no systematic analysis is made on the impact of these processes on the optical characteristics of the back contact. Optimization of these processes requires for back-contact configurations to keep a high degree of transparency and good electrical properties after fabrication of the solar cell, and this implies the need for a systematic analysis of the impact of the processes on the optical and electrical characteristics of the back-contact configurations.

In this framework, this work reports a detailed study of the stability of ITO-based back-contact configurations under the coevaporation processes that are developed for the synthesis of high-efficiency CIGSe solar cells. Previous works developed on chalcogenide device technologies closely related to CIGSe as kesterites (Cu₂ZnSn(S,Se)₄ compounds) have shown the potential of nanometric chalcogenide FLs such as MoSe₂ on TCO-based back contacts for the achievement of high-efficiency devices.[36] In this work, different bare ITO, ITO/Mo, ITO/MoSe₂, and ITO/MoS₂ back-contact configurations have been studied as the function of both the CIGSe synthesis temperature and the thickness of the FLs, and we have analyzed the impact of such back contacts on the optoelectronic properties of the CIGSe solar cells. The results show that bare ITO layers can be used as efficient back contacts for coevaporation process temperatures of 480 °C. However, higher process temperatures lead to the formation of an amorphous In–Se phase at the ITO surface that reduces drastically both the transparency of the contacts in the visible region and the efficiency of solar cells. Inclusion of Mo FL leads to the formation of MoSe₂ interfacial phase during the coevaporation process, and the presence of this phase has been observed to improve significantly the efficiency of the cells, achieving device efficiencies similar to those obtained with reference solar cells fabricated with standard Mo back contacts. Optimization of the thickness of the initial Mo layer also allows to improve the contact transparency, achieving contacts with an optical transparency of 50% in the visible region. This is also accompanied by a relevant decrease in back reflectivity in the CIGSe devices, confirming the potential of these contact configurations for the development of semitransparent CIGSe devices with improved optical aesthetic quality without compromising the device performance. Further optimization of the processes is required to achieve higher AVT values as required for higher-transparency devices and high-efficiency tandem device configurations. This gives interest to further research on alternative FLs as those based on MoO₃ nanometric layers, which show

ADVANCED
SCIENCE NEWS
www.advancedsciencenews.com

Solar
RRL
www.solar-rrl.com

interesting optical properties as recently reported from first simulation studies.[37]

2. Results and Discussion

2.1. Impact of Coevaporation Process Temperatures on ITO and ITO/MoSe₂ Back Contacts

The substitution of the standard metallic Mo back contact by semitransparent ITO and ITO/MoSe₂ back contacts was studied at different temperatures of the CIGSe coevaporation process to determine the impact of the temperature on such back contacts. In this section, and for all the process temperatures, MoSe₂ was obtained by depositing an ultrathin Mo metallic layer with a nominal thickness of 20 nm on the surface of the ITO contact, and this Mo layer was selenized in situ during the CIGSe coevaporation process.

Figure 1a shows the average visible transmittance (AVT), which is defined in **Equation (1)** in the Experimental Section, of mechanically exposed ITO and ITO/MoSe₂ back contacts as a function of the coevaporation process temperature. Reference (as-grown) ITO layers have a high level of transparency with a value of AVT around 80%. However, processing of the CIGSe layer leads to a decrease in AVT of the bare ITO back contact with the processing temperature, down to a value of 43% for the highest process temperature of 625 °C. In the case of the ITO/MoSe₂ back contacts, the AVT is much lower than the value obtained on the corresponding bare ITO back contact with the same CIGSe processing temperature, showing a minimum value of 22% for the lowest processing temperature of 480 °C. In this case, increasing the processing temperature leads to a gradual increase in AVT of the exposed contact, in contrast with the process temperature dependence obtained on the bare ITO back contacts.

Figure 1b shows the relative energy conversion efficiencies of CIGSe devices with ITO and ITO/MoSe₂ back contacts as a function of the coevaporation process temperature by normalizing to the efficiency achieved with a reference CIGSe single cell processed in the very same batch and using a standard Mo back

contact. It can be observed that the relative efficiency of the device with bare ITO back contact notably decreases with temperature, while the relative efficiency of the device with ITO/MoSe₂ back contact tends to increase when increasing the temperature. At highest temperatures, the relative efficiency of the device with ITO/MoSe₂ back contact is much higher than that of the device with bare ITO back contact.

Current density–voltage (J–V) curves are shown in Figure S1, Supporting Information, for the different temperatures. Table S1, Supporting Information, summarizes the main optoelectronic parameters of the devices. A clear current blocking behavior can be observed at 540 °C on the bare ITO sample, with a roll-over effect (current saturation at high forward bias).[38] This observation is discussed at the end of this section. So, in the case of bare ITO contacts, the worsening of the optical transparency is also accompanied by worsening of the optoelectronic properties of the CIGSe solar cells fabricated with these contacts. Only for the lowest process temperature of 480 °C, the solar cell shows a relative efficiency which corresponds to more than 80% of the efficiency achieved in the Mo-based reference devices. This, together with the high transparency of the layer (of 79%, as shown in Figure 1a), gives interest to the use of bare ITO back contacts for the fabrication of semitransparent CIGSe devices. However, the efficiency of the devices is limited by the low value of the process temperature, that is below 500 °C, and the efficiency of the reference solar cells produced with this process is of the order of 10% (Table S1, Supporting Information).

Achievement of high-efficiency CIGSe devices normally requires the use of process temperatures higher than 500 °C[39–42] and this is in particular the case with the baseline process using the Mo substrate, as described in the study by Jarzembowski et al.[43] This allows to increase the efficiency of the reference cells to values up to 15.6% (Table S1, Supporting Information). As shown in Figure 1b, the inclusion of an interfacial MoSe₂ layer between the CIGSe absorber and the ITO back contact allows to achieve contacts with good electrical properties, obtaining relative efficiency values higher than 80% obtained with the devices processed at 540 and 625 °C. However, the improvement of the optoelectronic properties is
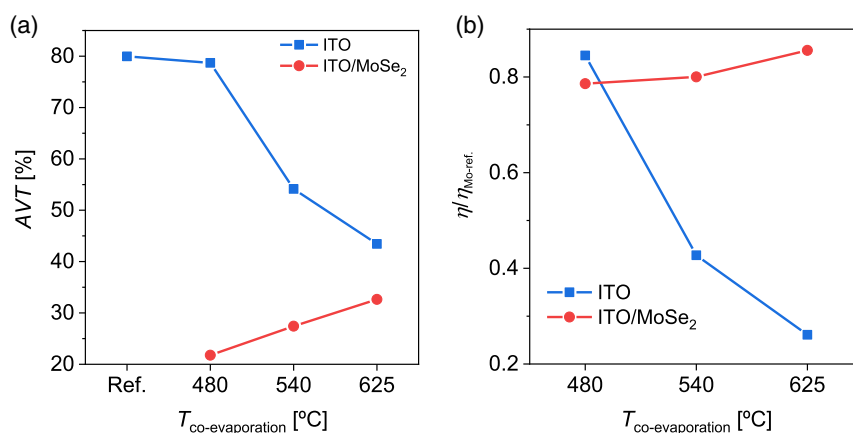

Figure 1. a) AVT of exposed ITO and ITO/MoSe₂ back contacts on glass substrate as a function of the coevaporation process temperature. Back contacts are exposed by mechanical removal of CIGSe and upper layers. b) Normalized energy conversion efficiency of CIGSe devices with ITO and ITO/MoSe₂ back contacts as a function of the coevaporation process temperature. Energy conversion efficiency values are normalized to those of a CIGSe device with a standard Mo back contact synthesized in the very same batch.

compromised by a strong reduction of the optical transparency with respect to that achieved with the bare ITO back contacts.

Figure 2 shows Raman spectra obtained on the exposed bare ITO and ITO/MoSe$_2$ back-contact surfaces as a function of the co-evaporation process temperature using 785 nm excitation wavelength. On the one hand, the Raman spectra (blue line) from the bare ITO back contacts are characterized by the presence of broad bands, and the most intense ones are located in between 400 and 600 cm^{-1} spectral region (with peaks at 433 and 550 cm^{-1}) and in between 200 and 300 cm^{-1} spectral region (with a peak at 225 cm^{-1}). Increasing the process temperature leads to a relevant increase in the intensity of the Raman bands. The presence of these bands indicates the formation of a surface phase that is likely located at the CIGSe/ITO interface, and the width of these Raman bands indicates a low level of crystallinity for this phase. In consideration with Figure 1a, the presence of this phase is likely responsible for the degradation of the transparency of the ITO layers. Increasing the processing temperature leads to an increase in the formation of this phase, as shown by the relevant increase in intensity of the Raman bands in the measured spectra, and this likely leads to the observed strong decrease in AVT of the bare ITO back contact with increasing processing temperature in Figure 1a.

The detected broad bands appear within the spectral regions that are characteristic of amorphous In–Se phases.[44–47] For the same chemical composition, Raman spectra of amorphous phases change notably with respect to the spectra of crystalline phases.[44,48] It has been reported that the amorphous In$_2$Se$_3$ presents a broad band with a peak at 255 cm^{-1} and a broad band with a peak at 490 cm^{-1},[44] while In$_x$Se$_{1-x}$ presents a broad band with a peak that ranges from 190 to 255 cm^{-1} depending on the In/Se ratio.[46] According to this, the Raman bands observed in Figure 2 for bare ITO back contacts have been attributed to the presence of an amorphous In–Se phase, and the composition of
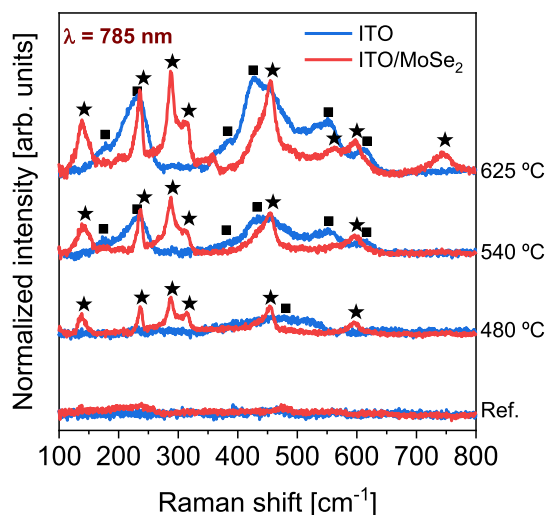
this phase is responsible of the changes of the bands in relation to those characteristic from stoichiometric In$_2$Se$_3$. This means that the surface of the ITO back contact is selenized during the coevaporation process, forming an amorphous In–Se phase at the ITO/CIGSe interface that reduces the transparency of the back contact and degrades the optoelectronic properties of the device. It is not known whether Sn or Ga atoms are incorporated into this amorphous phase. The presence of some CIGSe contribution to the Raman peak located at ≈175 cm^{-1} from residual CIGSe on the exposed back contact after the segmentation process cannot be excluded. However, the dependence of the intensity of this peak with the coevaporation process temperature strongly suggests this peak to be mainly related to the amorphous In–Se phase. This also agrees with the absence of this peak in the Raman spectra from the samples processed at 480 °C, where formation of the In–Se phase does not take place.

The detected Raman peaks do not correspond to the reported ones for Ga$_2$O$_3$ phase,[49,50] whose formation was suggested when growing CIGSe on ITO back contacts at high temperatures[9,28]; however, these results do not discard the Ga$_2$O$_3$ formation, as the used excitation wavelength is not optimum for the Raman detection of this phase.

On the other hand, the Raman spectra (red line) measured on the exposed ITO/MoSe$_2$ contacts show the presence of the Raman peaks characteristic of the MoSe$_2$ phase.[51] Note that the relative intensity of the peaks can be influenced using resonant excitation conditions,[51] possible preferential orientation of the MoSe$_2$ layer,[52] and/or by the nanometric thickness of this layer.[53] These measurements confirm the formation of MoSe$_2$ interfacial phase during the CIGSe coevaporation process due to the in situ selenization of the ultrathin Mo layer deposited on the ITO. Increasing the process temperature leads to an increase in the intensity of the peaks, and this is likely due to an increased thickness of the MoSe$_2$ layer formed during the process, in spite of the same thickness of the Mo layer in the as-grown ITO/Mo contacts. This indicates that for these process conditions the initial Mo layer is not fully selenized and there is a remaining Mo layer that is located between the MoSe$_2$ layer and the ITO contact. The presence of this Mo metallic layer would explain the strong decrease of the transparency of these contacts with respect to the bare ITO ones, as shown in Figure 1a. Increasing the process temperature leads to a decrease in the remaining Mo layer, related to the increase in the thickness of the MoSe$_2$ layer, and this explains the increase in transparency of these contacts with the process temperature.

Summarizing the impact of the CIGSe coevaporation process temperature on the semitransparent back contacts, it has been observed that bare ITO back contacts have an AVT of 79% after the coevaporation temperature at 480 °C and produce solar cells with relative efficiencies which correspond to more than 80% of the efficiency achieved using a standard Mo back contact. However, increasing the process temperature results in selenization of the ITO back contact, thus forming an amorphous In–Se at the back interface that decreases the AVT of the back contact and the efficiencies (mainly due to the V_{OC} and fill factor (FF)) of the devices. The presence of the In–Se phase could be responsible for a Schottky barrier at the back interface and would explain the roll-over effect observed.[38] At 625 °C, the J–V curve is perfectly linear, and the device behaves like a photoresistor. Such an

Figure 2. Raman spectra obtained on exposed bare ITO and ITO/MoSe$_2$ back contacts as a function of the coevaporation process temperature using 785 nm excitation wavelength. Star symbols indicate Raman peaks related to vibrational modes of MoSe$_2$ phase[51] and square symbols indicate Raman peaks related to an amorphous In–Se phase.[44–47] The spectra are normalized to the noise of the baseline.

observation can be related to either a high series resistance or low shunt resistance. As current and voltage are only marginally affected, it is currently not possible to discriminate between both hypotheses without additional material characterization. A thick, insulating, InSe layer could lead to a strong series resistance, while a small shunt resistance could be ascribed to process imperfections (pinholes) or metallic phases bypassing the p–n junction. In consequence, bare ITO does not appear suitable as a back contact for CIGSe devices fabricated at process temperatures of 540 °C or higher. At such high temperatures, the application of an ultrathin Mo layer on the ITO, that is selenized during the coevaporation process, thus forming an ITO/$MoSe_2$ back contact, prevents the degradation of both the transparency and the optoelectronic properties when increasing the process temperature, as clearly seen in the J–V curves. With this ITO/$MoSe_2$ back contact, relative efficiencies higher than 80% of those of a reference CIGSe device with a standard Mo back contact are achieved. However, though it is not degraded with process temperature, a remaining Mo layer reduces the optical transparency of the back contact, so it must be optimized for ensuring its viability for BIPV applications.

2.2. Thickness Control of FL on the ITO-Based Back Contacts Processed at 625 °C

According to the experimental data described in the previous section, optimization of the transparency of the ITO/$MoSe_2$ back contacts could be achieved by suitable tuning of the thickness of the initial Mo layer deposited onto the ITO back contact, trying to avoid the presence of a residual Mo metallic layer in the processed devices. To clarify this, the impact of the thickness of the initial Mo FL on the characteristics of the contacts has been investigated, using initial Mo FLs with nominal thicknesses between 10 nm and 30 nm. For the devices analyzed in this section, the CIGSe absorbers were grown using a coevaporation process temperature of 625 °C, which allows to achieve higher device efficiency values.

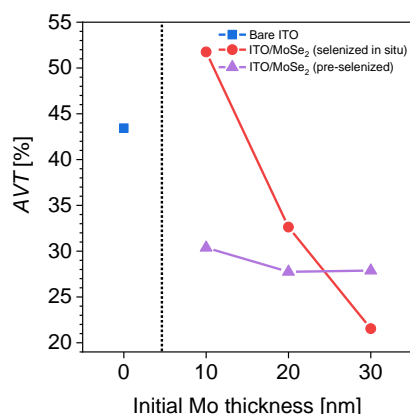**Figure 3** shows the AVT values measured after the solar cell process of the different mechanically exposed ITO/$MoSe_2$ back

Figure 3. AVT after the coevaporation process of exposed ITO/$MoSe_2$ back contacts as a function of the nominal thickness of the initial Mo layer. The AVT of an exposed bare ITO back contact processed with the same conditions is included.

contacts as a function of the initial Mo FL nominal thickness. As shown in this figure, decreasing the thickness of the Mo initial layer down to 10 nm allows to achieve, after the coevaporation process, a relevant increase in the transparency of the ITO/$MoSe_2$ contact selenized in situ (with an AVT value of 52%). This is likely related to the full selenization of the initial Mo layer. The transparency of this contact is also higher than the transparency achieved with the bare ITO contact (of about 43%). This suggests that the $MoSe_2$ interfacial layer that is formed in situ during the coevaporation process prevents the formation of a-In–Se phase on the ITO surface; in this case, the loss of transparency in relation to the bare ITO as-deposited layer is likely related to optical absorption in the nanometric $MoSe_2$ layer. Increasing the thickness of the initial Mo layer leads to a strong decrease in transparency, and this has been attributed to the presence of a remaining unreacted metallic Mo layer between the $MoSe_2$ layer and the ITO back contact for the FLs obtained with thicker Mo layers. This interpretation is supported by the Raman measurements performed on these layers, as shown later. It is worth noting that, even in the case of the fully selenized ITO/$MoSe_2$ back contact, no peeling problems were observed after CIGSe deposition. This might be related to the formation of a $MoSe_2$ layer with the crystalline c-axis parallel to the substrate.[54]

Synthesizing the $MoSe_2$ layer before the CIGSe coevaporation process leads to contacts with a transparency value that does not depend on the thickness of the layer. However, in this case, the transparency achieved is much lower than that obtained with the Mo thinnest layer that is selenized in situ during the coevaporation process, as the transparency values are in the range 28–30%. This behavior has been attributed to a degradation of the ITO surface during the selenization process that is performed before the coevaporation of the CIGSe absorber. This process is performed at a temperature of 500 °C during strongly selenizing conditions, which would explain the formation of ITO selenized phases at the surface of the ITO back contact.

Table 1 shows the average reflectance values measured in the visible spectral region on the back glass surface of the CIGSe devices fabricated with different ITO/$MoSe_2$ back contacts produced with an initial Mo layer thickness of 20 nm. The table shows also the values measured on the back glass surface from reference cells fabricated with a standard Mo back contact and from cells fabricated with a bare ITO back contact. It can be observed that the reflectance is reduced from a high value of 43.4% for standard Mo back contact to 9.1% for ITO/$MoSe_2$ back contact that is selenized in situ during the coevaporation process. In addition, the reflectance of the ITO/$MoSe_2$ back contact can be further reduced from 9.1% to 6.9% if the nanometric Mo layer is preselenized before the coevaporation process. Finally, a bare ITO back contact offers the lowest reflectance with 6.4%. This confirms the interest of these contact configurations for the

Table 1. Average reflectance measured in the visible spectral region (380–780 nm) from the back glass surface of CIGSe cells produced with different back-contact configurations.

Back contact	Glass/Mo (ref.)	Bare ITO	ITO/$MoSe_2$ (selenized in situ)	ITO/$MoSe_2$ (pre-selenized)
R [%]	43.4	6.4	9.1	6.9

ADVANCED
SCIENCE NEWS
www.advancedsciencenews.com

Solar
RRL

www.solar-rrl.com

improvement of the aesthetic quality of the CIGSe semitransparent devices, eliminating the "mirror effect" characteristic of the Mo back contact.

Figure 4a shows the Raman spectra measured with the 532 nm excitation wavelength at the back interface of CIGSe solar cells produced with ITO/MoSe$_2$ back contacts that are selenized in situ during the coevaporation process for different nominal thicknesses of the initial Mo layer. These spectra have been measured with the laser excitation spot on the back surface of the SLG substrate on complete solar cells. This has allowed to avoid potential damage effects in the measurements related to the mechanical removal of the CIGSe and upper layers. The presence of the peak at 238 cm^{-1} indicates that the Mo layers are always selenized, forming MoSe$_2$ at the CIGSe/back-contact interface.[51] However, the decrease of the absolute intensity of both the 176 and the 238 cm^{-1} peaks with the increase in the thickness of the initial Mo layer suggests the presence of a remaining metallic Mo that is likely located below the MoSe$_2$ layer. The thickness of this Mo metallic region increases with the nominal thickness of the initial Mo layer. This is in agreement with the observed decrease of the AVT for increasing thickness of the initial Mo layer shown in Figure 3. Figure 4b shows the Raman spectra measured in the same conditions from CIGSe solar cells with ITO/MoSe$_2$ back contacts that were preselenized

before the coevaporation deposition of the CIGSe layer. The presence of MoSe$_2$ (238 cm^{-1} peak)[51] is detected for samples with 20 and 30 nm initial Mo thickness, but not in the case of the 10 nm initial Mo layer. In this case, the thickness of the MoSe$_2$ FL is too low for efficient detection of the MoSe$_2$ peaks. Figure 4c shows the relative intensity of the MoSe$_2$ Raman peaks versus the nominal thickness of the initial Mo layer for all the processed ITO/MoSe$_2$ back contacts. For the MoSe$_2$ layers selenized in situ during the coevaporation process, the relative intensity of the MoSe$_2$ peaks is constant, which confirms that the thickness of the MoSe$_2$ layer produced during the coevaporation process is determined by the process parameters (i.e., the substrate temperature) but does not depend on the thickness of the initial Mo layer. This explains why for the thicker layers an unreacted metallic Mo layer remains below the selenized layer. This contrasts with the behavior observed for the MoSe$_2$ layers preselenized before the coevaporation process, where there is an increase in the thickness of the MoSe$_2$ layer with the thickness of the initial Mo layer.

Figure 5a shows the normalized energy conversion efficiencies of the CIGSe devices with different ITO-based back contacts as a function of the thickness of the initial Mo layer. It can be observed that in all cases there is relevant improvement in the efficiency of the devices in relation to the efficiency achieved using a bare ITO back contact. The highest efficiency values are achieved for the thickest initial Mo layers. Contrary to the case of the process temperature impact, the relative efficiency increase with increasing initial Mo layer thickness is due to an increase in J_{SC}, as shown in Figure 5b, while the V_{OC} and the FF remain more or less constant despite the thickness increase of the initial Mo layer (not shown). In the case of the Mo layers that are selenized in situ during the coevaporation process, the J_{SC} increase, and thus the relative efficiency increase, are likely related to the presence of a thicker Mo metallic layer below the MoSe$_2$ one, and this determines reduction of the sheet resistance of the back contact. In the case of the MoSe$_2$ layer that is selenized before the coevaporation process, this could be related to higher thickness of the MoSe$_2$ layer ensuring better coverage of the CIGSe/back-contact interface. Nevertheless, for all the investigated thicknesses of the initial Mo layer, the relative efficiency of the cells is higher than 80% of the efficiency of the reference CIGSe cells fabricated with a standard Mo back contact. This demonstrates the feasibility of these back-contact configurations to obtain devices with efficiencies similar to those achieved with standard Mo back contacts.

In addition to ITO/MoSe$_2$ back contacts, ITO/MoS$_2$ contacts have also been studied. Figure S2, Supporting Information, shows the AVT values obtained on contacts processed with MoS$_2$ FL. Use of a MoS$_2$ FL gives AVT and reflectance (see Table S2, Supporting Information) values similar to those obtained with the MoSe$_2$ layers selenized before the coevaporation process, even if in this case the AVT tends to decrease with the thickness in the FL. This behavior has been related to the existence of partial sulfurization of the initial Mo layer, which leads to a Mo metallic layer that is not selenized during the coevaporation process. This interpretation is supported by the Raman measurements (Figure S3, Supporting Information), which suggest a constant thickness of the MoS$_2$ layer independent of the initial thickness of the Mo layer. This behavior indicates the need to optimize the sulfurization process to ensure full sulfurization
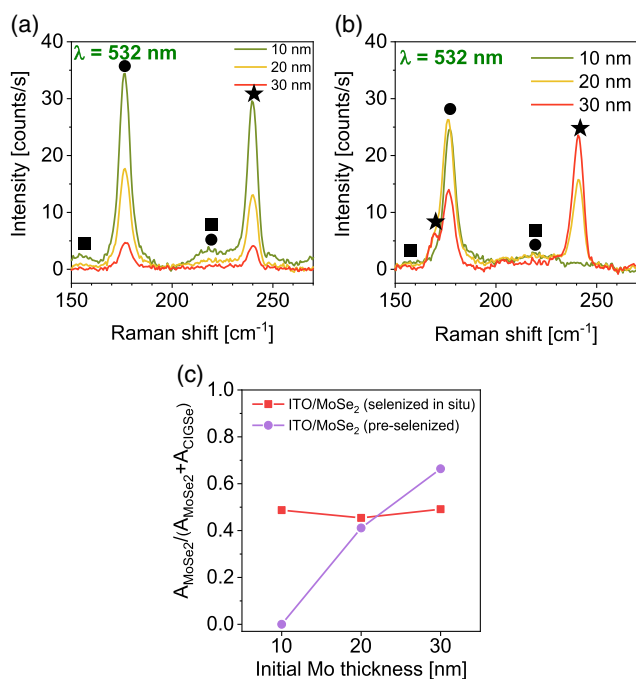

Figure 4. Raman spectra obtained using 532 nm excitation wavelength at the back interface of CIGSe solar cells synthesized at 625 °C with a) ITO/MoSe$_2$ (selenized in situ) and b) ITO/MoSe$_2$ (pre-selenized) back contacts for different initial Mo layers. Circle symbols indicate Raman peaks related to CIGSe vibrational modes, star symbols indicate peaks related to MoSe$_2$ vibrational modes, and square symbol indicates peaks related to vibrational modes of the CIGSe-ordered vacancy compounds. The back CIGSe/FL/ITO interface was analyzed by measuring the spectra with the laser spot on the back surface of the devices as the 532 nm wavelength was able to penetrate through the glass substrate. c) Relative area of the MoSe$_2$-related Raman peaks versus thickness of the initial Mo layer.
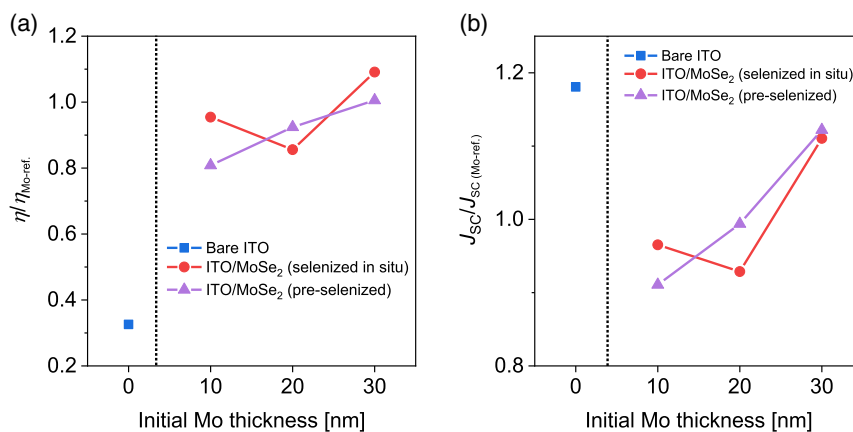
Figure 5. Normalized a) energy conversion efficiency and b) short-circuit current density of CIGSe devices with different ITO-based back contacts as a function of the thickness of the initial Mo layer. Optoelectronic parameters are normalized to those of a CIGSe device with a standard Mo back contact synthesized at the same conditions.

of the initial Mo layer. The presence of this Mo metallic region below the MoS_2 layer explains the low AVT values achieved within these contacts. On the other hand, the cells fabricated with the ITO/MoS_2 back contacts show device efficiencies similar to those achieved with $ITO/MoSe_2$ back contacts, as shown in Figure S4, Supporting Information.

Summarizing the impact of the FL thickness on the semi-transparent back contacts, it has been observed that, when selenizing the Mo layer applied on the ITO in situ during the coevaporation process, reducing the initial Mo layer thickness down to 10 nm allows to achieve an AVT of 52% while keeping energy conversion efficiency very close to that obtained with a standard Mo back contact. In this case, increasing the initial Mo layer thickness only increases the remaining metallic Mo layer thickness, not the $MoSe_2$ one, which drastically reduces the AVT of the back contact. If the initial Mo layer is preselenized before the CIGSe coevaporation process, the thickness of the formed $MoSe_2$ layer can be controlled by tuning the initial Mo layer thickness; however, this strategy produces low AVT values due to degradation of the ITO back contact during the preselenization process.

3. Conclusion

In conclusion, bare ITO layers can be used as back contacts with high transparency (close to 80%) in CIGSe devices coevaporated at temperatures $T \leq 480\,°C$. However, higher process temperatures lead to a partial selenization effect of the surface of the ITO layer, with the formation of an amorphous In–Se phase. This secondary phase leads to degradation of both the transparency in the visible region of the contacts and can also contribute to the observed degradation of the efficiency of the solar cells. This compromises the suitability of bare ITO back contacts for high-efficiency CIGSe semitransparent devices.

Inclusion of $MoSe_2$ or MoS_2 FLs on the surface of the ITO back contact allows a relevant improvement of the efficiency of the cells, leading to device efficiencies similar to those achieved with standard Mo back contacts, but processes have

to be finely tuned to avoid the presence of a remaining metallic Mo layer that would degrade the transparency of the contacts. In addition, $ITO/MoSe_2$ back contacts obtained by selenizing the Mo deposited layer before the CIGSe coevaporation process lead to low AVT values. This has been attributed to the deterioration of the ITO surface due to selenization of ITO as well. By tuning the thickness of the initial Mo layer to ensure its full selenization, AVT values up to 50% have been achieved using a 10 nm Mo FL that is selenized in situ during the coevaporation process. Finally, we are able to show that replacing the standard Mo back contact by ITO-based back contacts with and without FLs leads to a drastic decrease in the reflectance at the back surface of our devices, avoiding the "back-mirror" effect that hinders the aesthetic quality of CIGSe semitransparent devices fabricated with standard Mo back contacts.

4. Experimental Section

The synthesis process started with the sputtering deposition (Alliance Concept CT100) of the ITO (800 nm thick, sheet resistance $\approx 5\,\Omega.\square$) back contact on a SLG substrate laminated with a 100 nm SiN_x diffusion barrier. Then, a very thin layer of Mo (with a nominal thickness between 10 nm and 30 nm) was deposited by sputtering (Alliance Concept AC450).

Two strategies were used to obtain the $ITO/MoSe_2$ back contact. In the first case, the Mo layer deposited on ITO was selenized in situ during the CIGSe coevaporation process. In the second case, Mo was specifically selenized before the CIGSe coevaporation process. For the ITO/MoS_2 back contact, a similar procedure as in the latter case was followed. Selenization/sulfurization processes were both done within a tubular furnace and reactive annealing was performed at $500\,°C$ under an Ar atmosphere with a pressure of 1 bar and with the presence of elemental Se or S. The CIGSe coevaporation consisted of a three-stage process, described in the study by Jarzembowski et al,[43] with the second stage performed at very high temperature, that is, at 480, 540, or $625\,°C$ for the first experiment (synthesis temperature variation) and fixed at $625\,°C$ for the second one (FL thickness variation). Na was incorporated at the end of the growth process through NaF postdeposition treatment; this alkali incorporation strategy was previously optimized on Mo/glass substrates having an alkali-barrier layer, and the same process was transferred to the transparent substrates. The absorber layers were then completed into devices by depositing first a 50 nm-thick CdS layer (made by chemical bath deposition) and

followed with a 100–250 nm-thick i-ZnO/ITO window layer (Alliance Concept EVA 450) and a Ni/Al/Ni metal grid (E-gun Telemark 247).

Raman spectroscopy measurements were performed in a backscattering configuration though a probe designed at IREC using 532 and 785 nm lasers. The measurement spot size was ≈100 and 50 μm, respectively. For 785 nm excitation, an iHR 320 monochromator from Horiba Jobin Yvon coupled with a charge-coupled device (CCD) detector was used; for 532 nm excitation, a fHR 640 monochromator from Horiba Jobin Yvon coupled with an InGaAs detector was used. To avoid the presence of thermal effects in the spectra, excitation power density was kept below 50 W cm^{-2} in the laser spot. The measurements were performed at different surfaces of the samples. 1) The surface of exposed ITO-based back contacts was analyzed after performing mechanical removal of the CIGSe and upper layers in selected regions by scratching. To check if the process induced additional damage, selected samples were removed using a developed lift-off process using a microscope slide and an adhesive epoxy.[55] 2) The back CIGSe/FL/ITO interface was analyzed by measuring the spectra with the laser spot on the back surface of the devices as the used wavelengths were able to penetrate through the glass substrate. Configuration (2) had the advantage that measurements were not affected by potential damage effects related to the removal of the CIGSe top layer but were compromised by a lower signal-to-noise ratio.

Transmittance measurements were performed on the exposed regions of the ITO-based back contacts, after mechanical removal of the CIGSe and upper layers, using an light-emitting diode table and an iHR 320 monochromator from Horiba Jobin Yvon coupled with a CCD detector. The measurement spot size was ≈1 mm. Transmittance of exposed ITO-based back contacts was measured by illuminating the samples from the bottom side and the transmitted light was collected at the top side of the samples. The obtained transmittance spectra allowed to calculate the AVT, which is defined in Equation (1)

$$AVT = \frac{\int_{\lambda_1}^{\lambda_2} T(\lambda)P(\lambda)S(\lambda)d\lambda}{\int_{\lambda_1}^{\lambda_2} P(\lambda)S(\lambda)d\lambda} \qquad (1)$$

where λ is the wavelength, $T(\lambda)$ is the spectral transmissivity of the device evaluated, $P(\lambda)$ is the photopic response, $S(\lambda)$ is the solar photon flux (AM1.5G), and (λ_1, λ_2) is the integral range.[13,56,57] Analyzing the 435–670 nm range was sufficient to cover over 99% of the visible light spectrum[57]; in this work, the 380–780 nm range was analyzed as it was the optimum detection range of the system.

Reflectance measurements were performed using a Lambda 950 UV/VIS spectrometer from PerkinElmer coupled with a 150 mm integrating sphere from the same company. The total reflectance of the back contacts was measured from the glass substrate side, at regions where the CIGSe absorber was not removed. Average reflectance was also calculated in the 380–780 nm spectral range as the arithmetic mean of the reflectance values measured at each wavelength.

Optoelectronic properties of the solar cells were measured with a home-built sun simulator in a four-wire configuration. For electrical probing and sensing, a Keithley 2400 source meter was utilized. The electrical characterization of the solar cells took place under standard testing conditions (STCs), using a 3350 K tungsten halogen lamp calibrated to an intensity of 1 sun equivalent light.

Supporting Information

Supporting Information is available from the Wiley Online Library or from the author.

Conflict of Interest

The authors declare no conflict of interest.

Data Availability Statement

The data that support the findings of this study are available from the corresponding author upon reasonable request.

[1] M. Nakamura, K. Yamaguchi, Y. Kimoto, Y. Yasaki, T. Kato, H. Sugimoto, *IEEE J. Photovoltaics* **2019**, *9*, 1863.

[2] T. Feurer, P. Reinhard, E. Avancini, B. Bissig, J. Löckinger, P. Fuchs, R. Carron, T. P. Weiss, J. Perrenoud, S. Stutterheim, S. Buecheler, A. N. Tiwari, *Prog. Photovoltaics Res. Appl.* **2017**, *25*, 645.

[3] N. Cavallari, F. Pattini, S. Rampino, F. Annoni, M. Barozzi, M. Bronzoni, E. Gilioli, E. Gombia, C. Maragliano, M. Mazzer, G. Pepponi, G. Spaggiari, R. Fornari, *Appl. Surf. Sci.* **2017**, *412*, 52.

[4] M. J. Shin, A. Lee, A. Cho, K. Kim, S. K. Ahn, J. H. Park, J. Yoo, J. H. Yun, J. Gwak, D. Shin, I. Jeong, J.-S. Cho, *Nano Energy* **2021**, *82*, 105729.

[5] M. Mazzer, S. Rampino, G. Spaggiari, F. Annoni, D. Bersani, F. Bissoli, M. Bronzoni, M. Calicchio, E. Gombia, A. Kingma, F. Pattini, E. Gilioli, *Sol. Energy Mater. Sol. Cells* **2017**, *166*, 247.

[6] A. Mavlonov, T. Nishimura, J. Chantana, Y. Kawano, T. Masuda, T. Minemoto, *Sol. Energy* **2020**, *211*, 1311.

[7] Y.-J. Hsiao, T.-J. Hsueh, J.-M. Shieh, Y.-M. Yeh, C.-C. Wang, B.-T. Dai, W.-W. Hsu, J.-Y. Lin, C.-H. Shen, C. W. Liu, C. Hu, F.-L. Yang, in *2011 Int. Electron Devices Meet.*, IEEE, Washington **2011**, 36.5.1.

[8] M. Saifullah, S. Ahn, J. Gwak, S. Ahn, K. Kim, J. Cho, J. H. Park, Y. J. Eo, A. Cho, J.-S. Yoo, J. H. Yun, *J. Mater. Chem. A* **2016**, *4*, 10542.

[9] T. Nakada, Y. Hirabayashi, T. Tokado, D. Ohmori, T. Mise, *Sol. Energy* **2004**, *77*, 739.

[10] Z. Yu, M. Leilaeioun, Z. Holman, *Nat. Energy* **2016**, *1*, 16137.

[11] M. Elbar, S. Tobbeche, A. Merazga, *Sol. Energy* **2015**, *122*, 104.

[12] S. Ishizuka, *Phys. Status Solidi A* **2019**, *216*, 1800873.

[13] C. J. Traverse, R. Pandey, M. C. Barr, R. R. Lunt, *Nat. Energy* **2017**, *2*, 849.

[14] T. Miyazaki, A. Akisawa, T. Kashiwagi, *Renewable Energy* **2005**, *30*, 281.

[15] D. H. W. Li, T. N. T. Lam, K. L. Cheung, *Energy Convers. Manage.* **2009**, *50*, 1981.

[16] C. J. M. Emmott, J. A. Röhr, M. Campoy-Quiles, T. Kirchartz, A. Urbina, N. J. Ekins-Daukes, J. Nelson, *Energy Environ. Sci.* **2015**, *8*, 1317.

[17] R. Ciriminna, F. Meneguzzo, L. Albanese, M. Pagliaro, *Green* **2015**, *5*, 73.

[18] B. Petter Jelle, C. Breivik, H. Drolsum Røkenes, *Sol. Energy Mater. Sol. Cells* **2012**, *100*, 69.

[19] J.-H. Yoon, J. Song, S.-J. Lee, *Sol. Energy* **2011**, *85*, 723.

[20] M. A. Green, E. D. Dunlop, J. Hohl-Ebinger, M. Yoshita, N. Kopidakis, X. Hao, *Prog. Photovoltaics Res. Appl.* **2021**, *29*, 657.

[21] T. Matsui, A. Bidiville, K. Maejima, H. Sai, T. Koida, T. Suezaki, M. Matsumoto, K. Saito, I. Yoshida, M. Kondo, *Appl. Phys. Lett.* **2015**, *106*, 053901.

[22] Z. Li, T. Ma, H. Yang, L. Lu, R. Wang, *Sol. RRL* **2021**, *5*, 2000614.

[23] T. Sidali, A. Bou, D. Coutancier, E. Chassaing, B. Theys, D. Barakel, R. Garuz, P.-Y. Thoulon, D. Lincot, *EPJ Photovoltaics* **2018**, *9*, 2.

[24] D. Lee, K. Yong, *Korean J. Chem. Eng.* **2013**, *30*, 1347.

[25] M. Sibinski, K. Znajdek, *Solar Cells - Thin-Film Technologies*, InTech, London, United Kingdom **2011**.

[26] S. Calnan, *Coatings* **2014**, *4*, 162.

[27] N. Khoshsirat, N. A. M. Yunus, *Nanoelectronics and Materials Development*, InTech, London, United Kingdom **2016**.

[28] T. Nakada, *Thin Solid Films* **2005**, *480–481*, 419.

[29] Y. Li, G. Yin, M. Schmid, *Sol. Energy Mater. Sol. Cells* **2022**, *234*, 111431.

[30] K. Kim, W. N. Shafarman, *Nano Energy* **2016**, *30*, 488.

[31] S. Nishiwaki, S. Siebentritt, P. Walk, M. Ch Lux-Steiner, *Prog. Photovoltaics Res. Appl.* **2003**, *11*, 243.

[32] W. Ohm, W. Riedel, U. Aksunger, D. Greiner, C. A. Kaufmann, M. C. Lux-Steiner, S. Gledhill, in *2015 IEEE 42nd Photovolt. Spec. Conf.*, IEEE, New Orleans, LA **2015**, p. 1.

[33] J. Mattheis, P. J. Rostan, U. Rau, J. H. Werner, *Sol. Energy Mater. Sol. Cells* **2007**, *91*, 689.

[34] J. Keller, N. Shariati Nilsson, A. Aijaz, L. Riekehr, T. Kubart, M. Edoff, T. Törndahl, *Prog. Photovoltaics Res. Appl.* **2018**, *26*, 159.

[35] J. Keller, W.-C. Chen, L. Riekehr, T. Kubart, T. Törndahl, M. Edoff, *Prog. Photovoltaics Res. Appl.* **2018**, *26*, 846.

[36] I. Becerril-Romero, D. Sylla, M. Placidi, Y. Sánchez, J. Andrade-Arvizu, V. Izquierdo-Roca, M. Guc, A. Pérez-Rodríguez, S. Grini, L. Vines, B. Pusay, J. Puigdollers, P. Pistor, E. Saucedo, M. Espíndola-Rodríguez, *ACS Appl. Mater. Interfaces* **2020**, *12*, 33656.

[37] K. J. Tiwari, S. Giraldo, M. Placidi, A. Gon Medaille, A. Thomere, S. Resalati, E. Saucedo, Z. Jehl Li-Kao, *Sol. RRL* **2021**, *5*, 2100202.

[38] R. Scheer, H.-W. Schock, *Chalcogenide Photovoltaics: Physics, Technologies, and Thin Film Devices*, Wiley-VCH Verlag GmbH & Co. KGaA, Weinheim, Germany **2011**.

[39] W. Li, L. Yao, K. Li, X. Li, B. Yang, S. Xu, S. Shi, C. Yi, M. Chen, Y. Feng, W. Li, Z. Lu, C. Yang, *ACS Appl. Energy Mater.* **2020**, *3*, 4201.

[40] D. Rudmann, D. Brémaud, A. F. da Cunha, G. Bilger, A. Strohm, M. Kaelin, H. Zogg, A. N. Tiwari, *Thin Solid Films* **2005**, *480–481*, 55.

[41] P. Jackson, R. Wuerz, D. Hariskos, E. Lotter, W. Witte, M. Powalla, *Phys. Status Solidi RRL* **2016**, *10*, 583.

[42] T. Kato, J.-L. Wu, Y. Hirai, H. Sugimoto, V. Bermudez, *IEEE J. Photovoltaics* **2019**, *9*, 325.

[43] E. Jarzembowski, M. Maiberg, F. Obereigner, K. Kaufmann, S. Krause, R. Scheer, *Thin Solid Films* **2015**, *576*, 75.

[44] J. Weszka, P. Daniel, A. Burian, A. M. Burian, A. T. Nguyen, *J. Non-Cryst. Solids* **2000**, *265*, 98.

[45] C.-H. Ho, *Sci. Rep.* **2015**, *4*, 4764.

[46] I. Watanabe, T. Yamamoto, *Jpn. J. Appl. Phys.* **1985**, *24*, 1282.

[47] J. Weszka, P. Daniel, A. M. Burian, *Acta Phys. Pol. A* **2000**, *98*, 619.

[48] P. Pistor, R. Caballero, D. Hariskos, V. Izquierdo-Roca, R. Wächter, S. Schorr, R. Klenk, *Sol. Energy Mater. Sol. Cells* **2009**, *93*, 148.

[49] C. Kranert, C. Sturm, R. Schmidt-Grund, M. Grundmann, *Sci. Rep.* **2016**, *6*, 35964.

[50] Y. Wang, N. Li, P. Duan, X. Sun, B. Chu, Q. He, *J. Nanomater.* **2015**, *2015*, 1.

[51] D. Nam, J.-U. Lee, H. Cheong, *Sci. Rep.* **2015**, *5*, 17113.

[52] T. Sekine, M. Izumi, T. Nakashizu, K. Uchinokura, E. Matsuura, *J. Phys. Soc. Japan* **1980**, *49*, 1069.

[53] M. Placidi, M. Dimitrievska, V. Izquierdo-Roca, X. Fontané, A. Castellanos-Gomez, A. Pérez-Tomás, N. Mestres, M. Espindola-Rodriguez, S. López-Marino, M. Neuschitzer, V. Bermudez, A. Yaremko, A. Pérez-Rodríguez, *2D Mater.* **2015**, *2*, 035006.

[54] C. M. Ruiz, A. Pérez-Rodríguez, J. Arbiol, J. R. Morante, V. Bermúdez, *Phys. Status Solidi A* **2015**, *212*, 61.

[55] J. Andrade-Arvizu, R. F. Rubio, V. Izquierdo-Roca, I. Becerril-Romero, D. Sylla, P. Vidal-Fuentes, Z. J. Li-Kao, A. Thomere, S. Giraldo, K. Tiwari, S. Resalati, M. Guc, M. Placidi, *ACS Appl. Mater. Interfaces* **2022**, *14*, 1177.

[56] C. Yang, D. Liu, M. Bates, M. C. Barr, R. R. Lunt, *Joule* **2019**, *3*, 1803.

[57] R. R. Lunt, *Appl. Phys. Lett.* **2012**, *101*, 043902.